

# Responsivity Enhancement of Wafer-Bonded In<sub>0.53</sub>Ga<sub>0.47</sub>As Photo-Field-Effect Transistor on Si Substrate via Equivalent Oxide Thickness Scaling

Sung-Han Jeon, Dae-Hwan Ahn, Kyul Ko, Won Jun Choi, Jin-Dong Song, Woo-Young Choi,\* and Jae-Hoon Han\*

A high-responsivity photo-field-effect transistor (photo-FET) with a metal-oxide-semiconductor (MOS) structure is a promising technology for low-intensity light detection with its high gain and low operation voltage. To enhance their responsivity, the equivalent oxide thickness (EOT) scaling is one of the effective solutions, which is a common technology to improve the electrical properties of MOSFETs using higher-*k* insulators. Herein, the EOT scaling effect on the optoelectrical characteristics of photo-FETs using Al<sub>2</sub>O<sub>3</sub> and Al<sub>2</sub>O<sub>3</sub>/HfO<sub>2</sub> gate stacks is investigated. Thanks to the EOT scaling effect introducing Al<sub>2</sub>O<sub>3</sub>/HfO<sub>2</sub>, only the transconductance of the photo-FET is enhanced without any significant change in the photovoltaic effect and cavity effect. As a result, its responsivity is improved by up to 1.7 times. The results give a basic strategy of the EOT scaling effect for photo-FETs; thus, the EOT scaling with a higher-*k* insulator is a powerful solution for the high-performance InGaAs photo-FET requiring high responsivity in the short-wavelength infrared range.

Different photodetector structures are used in the SWIR range, such as PIN photodetectors, avalanche photodiodes (APDs), and phototransistors, often employing materials like indium-gallium-arsenide (InGaAs)<sup>[5]</sup> or germanium (Ge).<sup>[6]</sup> Among these options, APDs are preferred for detecting weak light due to their internal gain. However, they come with challenges like high operating voltage and excess noise.<sup>[7,8]</sup> Phototransistors, especially 2D or organic photo-field-effect transistors (photo-FETs), are promising alternatives due to their adjustable internal gain and low operating voltage.<sup>[9]</sup> However, these materials face difficulties in achieving high-performance and large-scale production for a broad SWIR range compatible with complementary metal oxide semiconductor (CMOS) platforms.<sup>[10]</sup> For mass production purposes,

In<sub>0.53</sub>Ga<sub>0.47</sub>As PIN photodetectors have been widely used for SWIR detection and have recently been integrated into CMOS-compatible platforms.<sup>[11,12]</sup> InGaAs APDs have also been extensively studied to enhance responsivity using their high internal gain. However, these APDs typically require cooling for low-intensity light detection due to their low bandgap, and specialized techniques like zinc diffusion are needed to achieve high breakdown voltage.<sup>[13]</sup>


Conversely, In<sub>0.53</sub>Ga<sub>0.47</sub>As photo-FETs, which can be seamlessly integrated into the Si CMOS platform through wafer bonding technology, have recently emerged as optical power monitors or photodetectors with low operating voltage. These devices offer remarkable responsivity and rapid response times, attributed to their elevated electron mobility.<sup>[12,14]</sup> Furthermore, in our previous research, the responsivity of photo-FETs with metal reflector gates in metal-oxide-semiconductor (MOS) structures was improved due to the cavity effect of an MOS structure compared to conventional Si gates.<sup>[15]</sup> For further performance enhancement, it is important to understand the effect of equivalent oxide thickness (EOT) scaling, a common technique to improve the electrical properties of MOSFETs. In this article, we investigated the EOT scaling of wafer-bonded photo-FETs with a metal reflector by introducing a metal/Al<sub>2</sub>O<sub>3</sub>/HfO<sub>2</sub>/InGaAs gate stack. Using this technique, we demonstrated a 1.7-times-higher responsivity compared with the Al<sub>2</sub>O<sub>3</sub> InGaAs photo-FET at 1.55 μm wavelength. Also, we thoroughly conducted an electrical

## 1. Introduction

Short-wavelength infrared (SWIR) detectors find extensive applications in various fields, including silicon (Si) photonics,<sup>[1]</sup> medical devices,<sup>[2]</sup> light detection and ranging sensors,<sup>[3]</sup> and quantum computing.<sup>[4]</sup> Achieving high-performance light detectors is crucial to capture a wide range of light intensities.

S.-H. Jeon, D.-H. Ahn, K. Ko, W. J. Choi, J.-D. Song, J.-H. Han  
Center for Opto-Electronic Materials and Devices  
Korea Institute of Science and Technology (KIST)  
Seoul 02792, Republic of Korea  
E-mail: hanjh@kist.re.kr

S.-H. Jeon, W.-Y. Choi  
Department of Electrical and Electronic Engineering  
Yonsei University  
Seoul 03722, Korea  
E-mail: wchoi@yonsei.ac.kr

 The ORCID identification number(s) for the author(s) of this article can be found under <https://doi.org/10.1002/pssa.202300664>.

© 2024 The Authors. physica status solidi (a) applications and materials science published by Wiley-VCH GmbH. This is an open access article under the terms of the Creative Commons Attribution-NonCommercial-NoDerivs License, which permits use and distribution in any medium, provided the original work is properly cited, the use is non-commercial and no modifications or adaptations are made.

DOI: 10.1002/pssa.202300664

and optical analysis of the photo-FETs with an  $\text{Al}_2\text{O}_3/\text{HfO}_2$  gate oxide to understand why the photocurrent is increased. Finally, we compared the responsivity of devices with various channel lengths and under different light irradiation conditions.

## 2. Experimental Section

The fabrication process flow of InGaAs photo-FETs with  $\text{Al}_2\text{O}_3$  or  $\text{Al}_2\text{O}_3/\text{HfO}_2$  gate oxide layers is illustrated in **Figure 1a**. The wafer-bonded III–V wafer, which consists of an unintentionally doped (UID) indium phosphide (InP) buffer layer (50 nm), a UID-In<sub>0.53</sub>Ga<sub>0.47</sub>As etching stop layer (200 nm), a UID-InP etching stop layer (50 nm), a heavily doped N + InGaAs source/drain (S/D) layer (50 nm) with a Si concentration of  $1 \times 10^{19} \text{ cm}^{-3}$ , and UID-InGaAs channel layer (50 nm), respectively, was grown on an InP (001) substrate by the molecular beam epitaxy method. The III–V wafer was imposed surface treatment with ammonia ( $\text{NH}_3$ ) solution for 2 min and ammonium sulfide  $[(\text{NH}_4)_2\text{S}_x]$  solution for 5 min to remove native oxide and achieve a high-quality MOS interface.<sup>[16,17]</sup> 1 nm-thick aluminum oxide/8 nm-thick hafnium oxide ( $\text{Al}_2\text{O}_3/\text{HfO}_2$ ) films were deposited by the atomic layer deposition (ALD) method, using trimethylaluminum  $[\text{Al}(\text{CH}_3)_3]$  and tetrakis(ethylmethylamino)hafnium  $[\text{Hf}(\text{N}(\text{CH}_3)(\text{CH}_2\text{CH}_3))_4]$  and water ( $\text{H}_2\text{O}$ ) as precursors. 1 nm-thick  $\text{Al}_2\text{O}_3$  was inserted between InGaAs and  $\text{HfO}_2$  to achieve the high-quality InGaAs MOS interface.<sup>[18]</sup> A 10 nm-thick  $\text{Al}_2\text{O}_3$  was also deposited for a control sample. We deposited similar thicknesses for  $\text{Al}_2\text{O}_3$  and  $\text{Al}_2\text{O}_3/\text{HfO}_2$  gate oxides to eliminate the difference in cavity effect. The deposited samples were annealed at 400 °C for 10 min to prevent void from the oxide layers.<sup>[19]</sup> Then, 10 nm-thick tungsten (W) and 60 nm-thick gold (Au) were deposited on a III–V wafer and 300 nm-thick silicon dioxide ( $\text{SiO}_2$ )/Si substrate. As mentioned before, we already reported that W/Au plays the role of the metal reflector to

enhance the cavity effect.<sup>[15]</sup> The III–V and Si wafers were activated by argon (Ar) plasma and then directly bonded under pressure of  $\approx 0.25 \text{ MPa}$  at 200 °C for 1 h. The InP substrate was removed with polishing and diluted hydrochloric acid (HCl) solution. The InGaAs and InP etching stop layers were eliminated by the selective wet etching process with  $\text{HCl}:\text{H}_2\text{O}_2:\text{H}_2\text{O}$  (1:1:10) and  $\text{H}_3\text{PO}_4:\text{HCl}$  (3:1) solutions, respectively. The device patterning process was performed in the top-down etching process. The N + InGaAs S/D and UID-InGaAs channel layers were selectively etched in  $\text{H}_3\text{PO}_4$  solution due to the inserted InP etching stop layer. This thin etching stop layer was eliminated by  $\text{HCl}:\text{H}_3\text{PO}_4$  solution. Each device was isolated by wet and dry etching. The native oxide was eliminated by immersing dilute HCl solution for 1 min, and 30 nm-thick  $\text{Al}_2\text{O}_3$  was deposited with the ALD for field oxide (FOX). The  $\text{Al}_2\text{O}_3$  on the S/D region was etched by buffered oxide etchant solution to connect N+InGaAs S/D and Mo/Au Pad. The 20 nm molybdenum (Mo)/200 nm Au was deposited with the e-beam evaporator to form a contact pad. Finally, each sample was annealed at 250 °C for 1 min to achieve low contact resistance and alleviate the fixed charge in FOX film. **Figure 1b** shows a schematic diagram of a photo-FET illuminated by a SWIR light source. The optical image of photo-FET with  $\text{Al}_2\text{O}_3$  and  $\text{Al}_2\text{O}_3/\text{HfO}_2$  gate oxide is shown in **Figure 1c**.

## 3. Result and Discussion

First, the electrical characteristics of the fabricated InGaAs photo-FETs integrated on the Si substrate were investigated using a semiconductor parameter analyzer (Hewlett Packard 4156A) and LCR meter (Hewlett Packard 4284A), as shown in **Figure 2**. The black and red line indicates the electrical characteristics of photo-FETs with  $\text{Al}_2\text{O}_3$  and  $\text{Al}_2\text{O}_3/\text{HfO}_2$  gate oxide layers, respectively. The  $I_{\text{ds}}-V_{\text{gs}}$  curves of InGaAs photo-FETs were plotted in **Figure 2a**, showing that the  $\text{Al}_2\text{O}_3/\text{HfO}_2$  gate oxide exhibits higher on-current rather than the  $\text{Al}_2\text{O}_3$  gate oxide

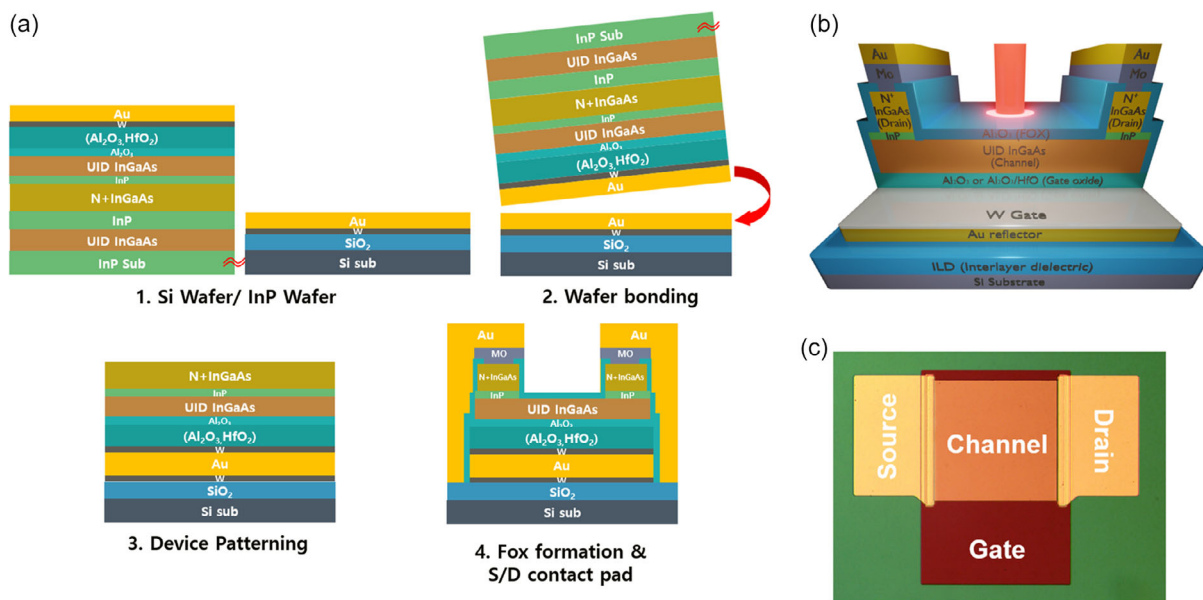


**Figure 1.** a) Process flow of  $\text{In}_{0.53}\text{Ga}_{0.47}\text{As}$  photo-FET on Si substrate. b) Schematic image of a photo-FET. c) Microscopic image of a fabricated photo-FET on Si substrate.

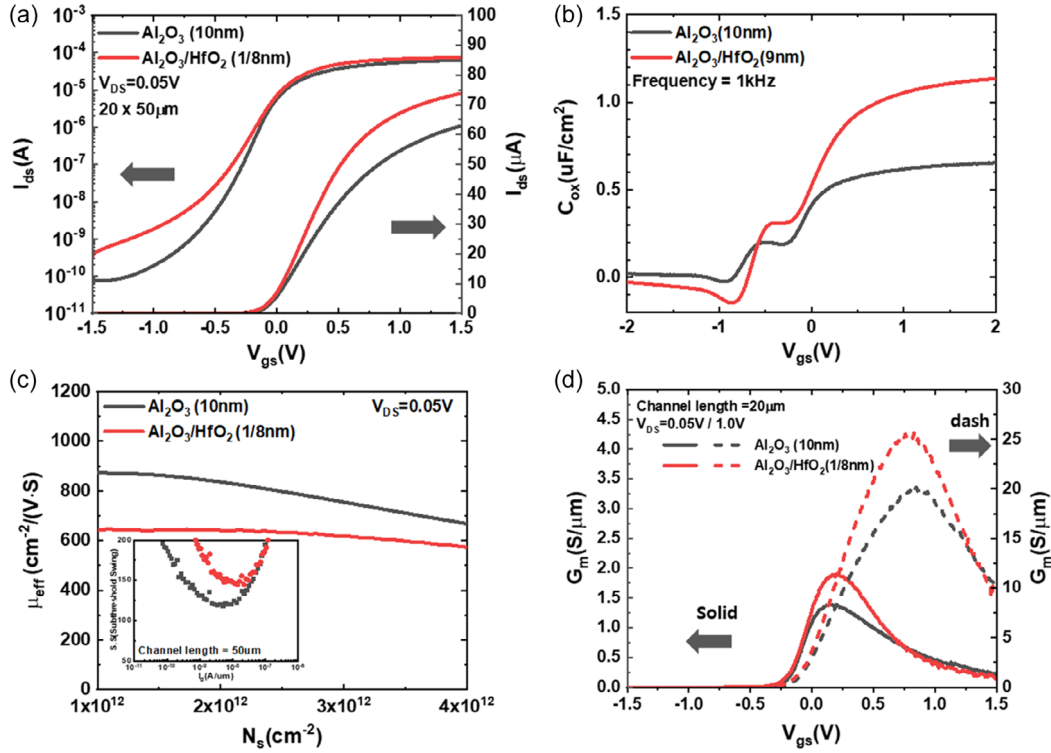


**Figure 2.** Electrical characteristics of InGaAs photo-FET with  $\text{Al}_2\text{O}_3$  and  $\text{Al}_2\text{O}_3/\text{HfO}_2$  gate oxide. a)  $I_{ds}$ - $V_{gs}$  curve, b)  $C_{ox}$ - $V_{gs}$  curve, c)  $\mu_{\text{eff}}$ - $N_s$  curve, and d)  $G_m$ - $V_{gs}$  curve.

due to its higher dielectric constant. Figure 2b shows the gate-to-channel capacitance ( $C_{gc}$ ) of each device, measured by the split  $C$ - $V$  measurement method. To remove parasitic capacitance caused by the overlap between the gate and source/drain regions, the oxide capacitance ( $C_{ox}$ ) was extracted by subtracting the total capacitance of a  $50 \times 100 \mu\text{m}^2$  device from a  $100 \times 100 \mu\text{m}^2$  device. The  $C_{ox}$  of the  $\text{Al}_2\text{O}_3/\text{HfO}_2$  gate oxide is 1.8 times higher than that of the  $\text{Al}_2\text{O}_3$  gate oxide. Figure 2c shows the relationship between the effective mobility and surface charge density ( $\mu_{\text{eff}}$ - $N_s$ ) of InGaAs photo-FETs using the following Equation (1):

$$\mu_{\text{eff}} = \frac{I_{ds}L}{WC_{ox}(V_{gs} - V_{th})V_{ds}} \quad (1)$$

$$N_s = \frac{C_{ox}(V_{gs} - V_{th})}{q}$$

where  $I_{ds}$  is the drain-to-source current,  $L$  is the channel length,  $W$  is the channel width,  $V_{gs}$  is the gate-to-source voltage,  $V_{ds}$  is the drain-to-source voltage,  $V_{th}$  is the threshold voltage of each device, and  $q$  is the elementary charge.

The InGaAs photo-FET with  $\text{Al}_2\text{O}_3/\text{HfO}_2$  gate oxide presents an effective mobility of  $643 \text{ cm}^{-2} (\text{V s})^{-1}$ , which is 1.4 times lower than  $872 \text{ cm}^{-2} (\text{V s})^{-1}$  for photo-FET with  $\text{Al}_2\text{O}_3$  gate oxide at a surface concentration of  $1 \times 10^{12} \text{ cm}^{-2}$ . This result is attributed to the increased scattering issue at the stronger gate electric field<sup>[20]</sup> and is due to the unoptimized MOS interface. In the equivalent MOS interface of  $\text{Al}_2\text{O}_3$  and  $\text{Al}_2\text{O}_3/\text{HfO}_2$  gate oxide, it is expected that the effective mobility of the same level or higher can be achieved.<sup>[21]</sup> Generally, the effective mobility at

the high electric field is degraded by the unintentional scattering, in the case of extremely thin EOT<sup>[22]</sup>, thus, further engineering, such as the superior MOS interface quality, is necessary to achieve the high-performance photo-FET with  $\text{Al}_2\text{O}_3/\text{HfO}_2$  gate oxide. Also, the transconductance ( $G_m$ ) of photo-FET is an important factor in determining the performance of analog circuits and photoresponsivity. Figure 2d shows the  $G_m$ - $V_{gs}$  curve of InGaAs photo-FETs with  $\text{Al}_2\text{O}_3/\text{HfO}_2$  and  $\text{Al}_2\text{O}_3$  gate oxides. The photo-FET with  $\text{Al}_2\text{O}_3/\text{HfO}_2$  achieves a larger transconductance that is 1.3 times greater than photo-FET with  $\text{Al}_2\text{O}_3$  thanks to the EOT scaling effect. Consequently, the  $I_{ds}$ - $V_{gs}$ ,  $C_{ox}$ - $V_{gs}$ ,  $\mu_{\text{eff}}$ - $N_s$ , and  $G_m$ - $V_{gs}$  show general electrical characteristics applied to EOT scaling, which gate oxide changes to the higher- $k$  dielectric.

The photocurrent ( $I_{ph}$ ) characteristics of photo-FET with  $\text{Al}_2\text{O}_3$  and  $\text{Al}_2\text{O}_3/\text{HfO}_2$  were investigated under illumination using a  $1.55 \mu\text{m}$  wavelength light source. Figure 3a shows an optical measurement setup based on a confocal microscope. The laser beam was concentrated at the center of the channel region, as shown in the inset image. This spot size is smaller than the  $10 \mu\text{m}$  channel region since the calculated Airy disk diameter of  $6.3 \mu\text{m}$ ; thus, the whole beam is included in the channel area. Figure 4b shows the  $I_{ds}$ - $V_{gs}$  characteristics of the photo-FETs with  $\text{Al}_2\text{O}_3$  and  $\text{Al}_2\text{O}_3/\text{HfO}_2$  gate oxide under a dark state to a light illumination state where its power is  $155.86 \mu\text{W}$ . An increased drain current was observed as the light power was increased. We also calculated the photocurrent ( $I_{ph} = I_{\text{illumination}} - I_{\text{dark}}$ ) of the photo-FETs with various channel lengths. Figure 4c shows  $I_{ph}$ - $V_{gs}$  characteristics of the photo-FETs with  $\text{Al}_2\text{O}_3$  and  $\text{Al}_2\text{O}_3/\text{HfO}_2$  gate oxide, where dot and straight line are

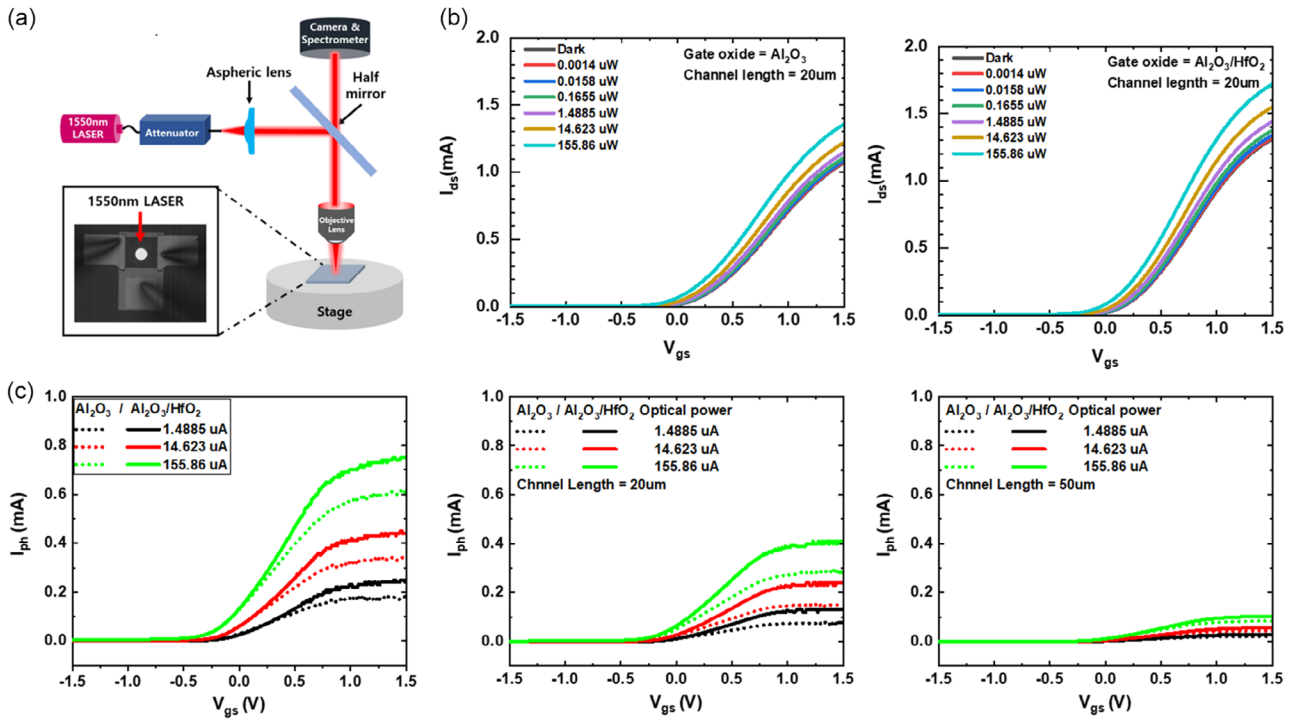


**Figure 3.** a) The confocal microscopy image. b)  $I_{ds}$ - $V_{gs}$  of photo-FET with  $\text{Al}_2\text{O}_3$  and  $\text{Al}_2\text{O}_3/\text{HfO}_2$  gate oxide. c) Comparison of  $I_{ph}$ - $V_{gs}$  in various channel lengths condition.

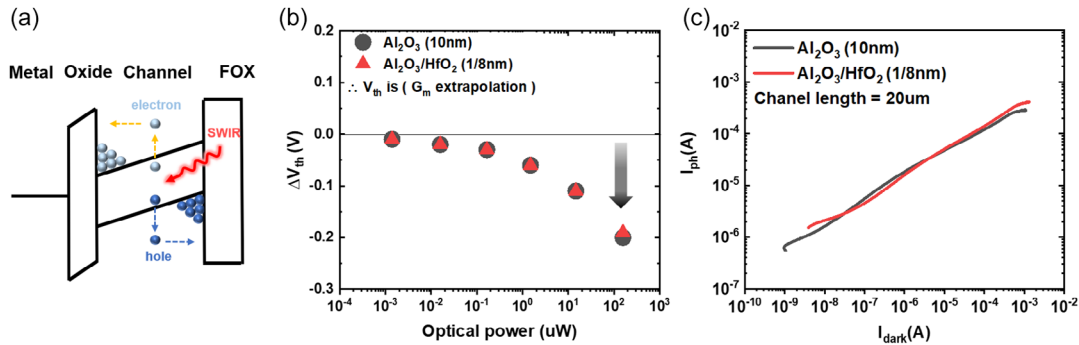


**Figure 4.** a) Band diagram of photo-FET through the vertical cross-sectional direction in on-state. b) Relationship between threshold voltage shift ( $\Delta V_{th}$ ) and irradiated optical power. c) Relationship between photocurrent ( $I_{ph}$ ) and dark current ( $I_{dark}$ ) of photo-FETs with  $\text{Al}_2\text{O}_3$  and  $\text{Al}_2\text{O}_3/\text{HfO}_2$  gate stacks.

photocurrent of  $\text{Al}_2\text{O}_3$  and  $\text{Al}_2\text{O}_3/\text{HfO}_2$ , respectively. The photocurrent was more increased as channel length decreased. These results are clearly understood through Equation (2), the increase of photocurrent is based on increased conductance due to the decreased channel length. Also, we observed that the photocurrent of  $\text{Al}_2\text{O}_3/\text{HfO}_2$  gate oxide is larger than  $\text{Al}_2\text{O}_3$  for all devices.

To understand these results, we will discuss the mechanism of photocurrent generation of a photo-FET device based on the photovoltaic effect.<sup>[23–25]</sup> As shown in Figure 4a, photo-generated electron–hole pairs in the channel region are separated under the applied electric field at the gate and accumulated on both channel sides. The photo-generated electrons are relatively flowing from the channel region to the drain region under the applied drain bias as electron mobility in the InGaAs channel is much

faster than the hole. In contrast, photo-generated holes are relatively stacked in the channel body or source edge because of their low effective mobility compared to electrons; thus, the threshold voltage ( $V_{th}$ ) is reduced, and more photocurrent is generated. When the device is in the on-state ( $V_{gs} > V_{th}$ ), the photocurrent generated by the photovoltaic effect is shown in Equation (2):

$$I_{ph,pv} = \frac{\partial I_{ds}}{\partial V_{gs}} \Delta V_{gs} = G_m \Delta V_{th} \quad (2)$$

$$G_m = \frac{W}{L} \mu_{eff} C_{ox} V_{ds}$$

where  $I_{ph,pv}$  is the photocurrent by photovoltaic effect,  $G_m$  is the transconductance defined by  $dI_{ds}/dV_{gs}$ ,  $\Delta V_{th}$  is a negative shift of

the threshold voltage,  $W/L$  is the channel width/length,  $\mu_{\text{eff}}$  is the effective mobility,  $C_{\text{ox}}$  is the gate capacitance, and  $V_{\text{ds}}$  is the drain voltage. As shown in Equation (2), the  $G_m$  and  $V_{\text{th}}$  are important factors to enhance the photocurrent. Especially, in the case of the photo-FET with  $\text{Al}_2\text{O}_3/\text{HfO}_2$  gate stack, improved photocurrent was observed owing to its high transconductance, as shown in Figure 2d.

However, to evaluate photocurrent accurately, we must also consider the threshold voltage shift, in addition to the increase in transconductance, as described in Equation (2). Therefore, we also investigated whether changed gate oxide material influences the cavity effect due to the variation of the gate dielectric constant. The threshold voltage shifts ( $\Delta V_{\text{th}}$ ) are induced by accumulated holes at the body and source edge. The photocurrent ( $I_{\text{ph}}$ ) and threshold voltage shift ( $\Delta V_{\text{th}}$ ) were investigated using a 20  $\mu\text{m}$ -long channel length. Figure 4b shows the  $V_{\text{th}}$  shift in various optical powers. The black and red dots are photo-FET with  $\text{Al}_2\text{O}_3$  and  $\text{Al}_2\text{O}_3/\text{HfO}_2$  gate oxide. Two photo-FET devices show the same variation of threshold voltage ( $V_{\text{th}}$ ). Figure 4c plots dark current ( $I_{\text{dark}}$ )–photocurrent ( $I_{\text{ph}}$ ) for both devices. The weakly changed photocurrent in the equivalent dark current is that the changed dielectric material has little effect on cavity effect enhancement in the channel. Consequently, we confirmed that the improved photocurrent has no direct relevance to the threshold voltage shift, or cavity effect based on changed dielectric constraints.

Additionally, the optical simulation with finite-difference time-domain method was carried out to understand the absorption behavior in the photo-FET with the MOS cavity using COMSOL Multiphysics because it is difficult to measure the absorption in the thin InGaAs channel directly. The detailed simulation method is the same as our previous article.<sup>[15]</sup> Figure 5a shows the schematic of simulated photo-FETs. To evaluate the influence of the gate oxides, the thicknesses and reflective indices of  $\text{Al}_2\text{O}_3$  and  $\text{Al}_2\text{O}_3/\text{HfO}_2$  were changed according to experimental values measured by ellipsometry. For simplicity, in the case of  $\text{Al}_2\text{O}_3/\text{HfO}_2$  gate oxide, we considered it to be one oxide layer with a refractive index of 2.0. As shown in Figure 5b, the reflectance of photo-FETs is not changed by the EOT scaling in this experiment because there are no differences in physical thickness and reflective index. The simulated absorption in the entire MOS cavity and InGaAs is also shown in Figure 5c. We could not observe a significant difference in the absorption

rate between the two samples for the MOS structure and InGaAs channel. From these results, we conclude that there is no significant enhancement in absorption by the EOT scaling, which is well matched with the opto-electrical measurement, as discussed in Figure 4.

Figure 6 shows the responsivity of photo-FET with  $\text{Al}_2\text{O}_3$  and  $\text{Al}_2\text{O}_3/\text{HfO}_2$  gate oxide of various channels and optical powers. The responsivity of each device was calculated by following Equation (3):

$$\text{Responsivity } (R) = \frac{I_{\text{ph}}}{P_{\text{in}}} \quad (3)$$

where  $P_{\text{in}}$  is optical input power. Figure 6a shows the responsivity of the device with 10, 20, and 50  $\mu\text{m}$  channel lengths. Figure 6b shows the responsivity from a feeble to a strong illumination state for devices of 20  $\mu\text{m}$  channel length. As shown in the figures, the device with  $\text{Al}_2\text{O}_3/\text{HfO}_2$  gate oxide shows higher responsivity thanks to its improved transconductance as discussed before. Furthermore, the decrease in responsivity under higher optical power can be attributed to the dominant photovoltaic effects in the on-state. This effect results in nonlinear growth of photocurrent with an increase in optical power<sup>[26]</sup>; thus, the responsivity is decreased at strong light irradiation. Figure 6c shows the benchmark of responsivity among our  $\text{Al}_2\text{O}_3$  and  $\text{Al}_2\text{O}_3/\text{HfO}_2$  photo-FETs, InAs QW Photo-FET,<sup>[14]</sup> InGaAs Photo-FET,<sup>[26]</sup> InGaAs PDs,<sup>[27]</sup> and extended InGaAs PD.<sup>[28]</sup> In the case of detectivity, we previously reported up to  $10^{12} \text{ cmHz}^{-1/2} \text{ W}$  in the case of  $\text{Al}_2\text{O}_3$  photo-FET<sup>[15]</sup>; however, further comprehensive investigation on the detectivity with EOT scaling is necessary. Also, we confirmed the rising and falling time under 0.2 and 1.0 ms for these devices, respectively; however, there is no significant EOT dependency (not shown). Therefore, further investigation into the relationship between speed and structure parameters such as EOT, gate length, and width is also necessary. In conclusion, the EOT scaling is also useful to enhance the responsivity of photo-FET.

## 4. Conclusion

We have demonstrated wafer-bonded  $\text{In}_{0.53}\text{Ga}_{0.47}\text{As}$  photo-FET with a metal gate reflector using direct wafer bonding technology for Si CMOS ROIC integration. The  $\text{Al}_2\text{O}_3/\text{HfO}_2$  gate stack was

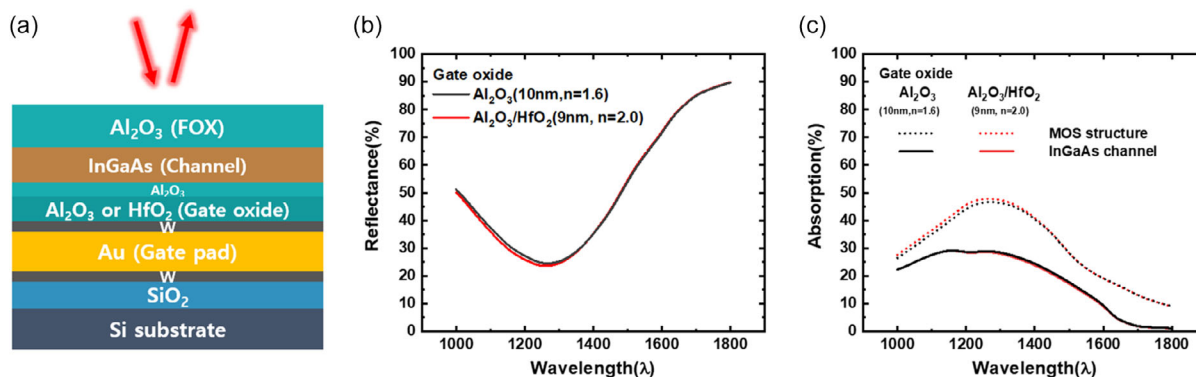


**Figure 5.** a) Sample schematic for simulation. b) The reflectance and c) absorption simulation of photo-FET with  $\text{Al}_2\text{O}_3$  and  $\text{Al}_2\text{O}_3/\text{HfO}_2$ .

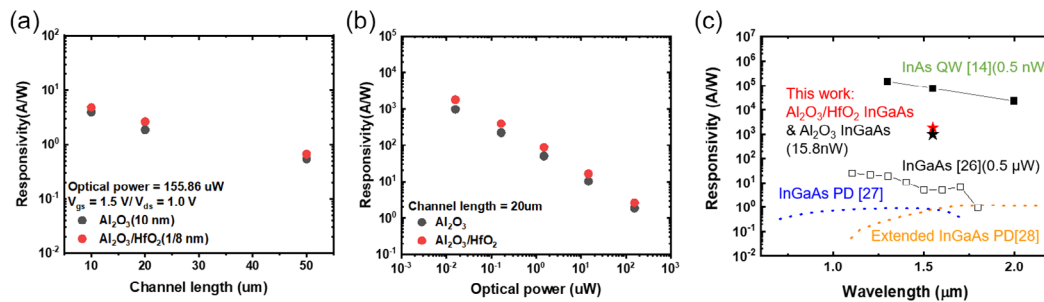


**Figure 6.** Responsivity for the photo-FET with  $\text{Al}_2\text{O}_3$  and  $\text{Al}_2\text{O}_3/\text{HfO}_2$  gate oxide in a) various channel lengths and b) optical powers. c) Benchmark of responsivity of our  $\text{Al}_2\text{O}_3$  and  $\text{Al}_2\text{O}_3/\text{HfO}_2$  photo-FETs, InAs QW Photo-FET,<sup>[14]</sup> InGaAs Photo-FET,<sup>[26]</sup> InGaAs photodiodes (PDs),<sup>[27]</sup> and extended InGaAs PD.<sup>[28]</sup>

introduced to enhance the electrical performance of photo-FET. Its transconductance was improved up to 1.4 times higher compared to the  $\text{Al}_2\text{O}_3$  control gate stack. The enhancement in photocurrent was also confirmed with the  $\text{Al}_2\text{O}_3/\text{HfO}_2$  gate stack compared to the  $\text{Al}_2\text{O}_3$  gate stack because the transconductance is one of the main factors of the gain of photo-FET. We also discussed the influence of the photovoltaic effect in this system, which is another main factor of its gain. There is no significant difference in the photovoltaic  $V_{th}$  shift and simulated absorption in the InGaAs channel layer. From these results, the cavity effect in this experiment is not affected by the EOT scaling; thus, we conclude that enhancement in transconductance is only the main factor of performance enhancement. We believe these results are useful for understanding the EOT scaling effect on the InGaAs photo-FET to achieve a high-performance SWIR detector.

## Acknowledgements

S.-H.J. and D.-H.A. contributed equally to this work. This research was partially supported by the National Research Foundation of Korea (NRF-2022M3F3A2A01065057, 2022R1C1C1007333), Korea Institute of Science and Technology (2E32942), and Institute for Information and Communication Technology Promotion (2022-0-00208).

## Conflict of Interest

The authors declare no conflict of interest.

## Data Availability Statement

The data that support the findings of this study are available on request from the corresponding author. The data are not publicly available due to privacy or ethical restrictions.

## Keywords

EOT scaling, III–V and Si integration, InGaAs, photo-FET, SWIR detector

Received: August 31, 2023

Revised: January 1, 2024

Published online: February 2, 2024

- [1] A. H. Atabaki, S. Moazeni, F. Pavanello, H. Gevorgyan, J. Notaros, L. Alloatti, M. T. Wade, C. Sun, S. A. Kruger, H. Meng, K. Al Qubaisi, I. Wang, B. Zhang, A. Khilo, C. V. Baiocco, M. A. Popović, V. M. Stojanović, R. J. Ram, *Nature* **2018**, 556, 349.
- [2] T. J. Huppert, S. G. Diamond, M. A. Franceschini, D. A. Boas, *Appl. Opt.* **2009**, 48, D280.
- [3] Y. Li, J. Ibanez-Guzman, *IEEE Signal Process. Mag.* **2020**, 37, 50.
- [4] X. Yan, S. Gitt, B. Lin, D. Witt, M. Abdolahi, A. Affi, A. Azem, A. Darcie, J. Wu, K. Awan, M. Mitchell, A. Pfenning, L. Chrostowski, J. F. Young, *APL Photonics* **2021**, 6, 070901.
- [5] Y. Liu, S. R. Forrest, J. Hladky, M. J. Lange, G. H. Olsen, D. E. Ackley, *J. Lightwave Technol.* **1992**, 10, 182.
- [6] D. Marris-Morini, V. Vakarin, J. M. Ramirez, Q. Liu, A. Ballabio, J. Frigerio, M. Montesinos, C. Alonso-Ramos, X. Le Roux, S. Serna, D. Benedikovic, D. Chrastina, L. Vivien, G. Isella, *Nanophotonics* **2018**, 7, 1781.
- [7] L. J. J. Tan, D. S. G. Ong, J. S. Ng, C. H. Tan, S. K. Jones, Y. Qian, J. P. R. David, *IEEE J. Quantum Electron.* **2010**, 46, 1153.
- [8] J. J.-S. Huang, H. S. Chang, Y.-H. Jan, C. J. Ni, H. S. Chen, E. Chou, *Adv. Optoelectron.* **2017**, 2017, 2084621.
- [9] D. Kufer, G. Konstantatos, *ACS Photonics* **2016**, 3, 2197.
- [10] B. Szlag, K. Hassan, L. Adelmini, E. Ghegin, P. Rodriguez, F. Nemouchi, P. Brianceau, E. Vermande, A. Schembri, D. Carrara, P. Cavalie, F. Franchin, M.-C. Roure, L. Sanchez, C. Jany, S. Olivier, *IEEE J. Sel. Top. Quantum Electron.* **2019**, 25, 1–10.
- [11] S. Manda, R. Matsumoto, S. Saito, S. Maruyama, H. Minari, T. Hirano, T. Takachi, N. Fujii, Y. Yamamoto, Y. Zaizen, H. Iwamoto, in *2019 IEEE Int. Electron Devices Meeting (IEDM)*, IEEE, Piscataway, NJ, December 2019, pp. 16.7.1–16.7.4, <https://doi.org/10.1109/IEDM19573.2019.8993432>.
- [12] T. Ochiai, T. Akazawa, Y. Miyatake, K. Sumita, S. Ohno, S. Monfray, F. Boeuf, K. Toprasertpong, S. Takagi, M. Takenaka, *Nat. Commun.* **2022**, 13, 7443.
- [13] J. Zhang, M. A. Itzler, H. Zbinden, J.-W. Pan, *Light: Sci. Appl.* **2015**, 4, e286.
- [14] D. H. Ahn, S. Jeon, H. Suh, S. Woo, R. J. Chu, D. Jung, W. J. Choi, D. Park, J.-D. Song, W.-Y. Choi, J.-H. Han, *Photonics Res.* **2023**, 11, 1465.
- [15] S. Kang, D. H. Ahn, I. Lee, W. J. Choi, J. Song, J.-H. Han, *Opt. Express* **2021**, 29, 42630.
- [16] S.-H. Yoon, K. Kato, C. Yokoyama, D.-H. Ahn, M. Takenaka, S. Takagi, *J. Appl. Phys.* **2019**, 126, 184501.
- [17] P. K. Hurley, E. O'connor, V. Djara, S. Monaghan, I. M. Povey, R. D. Long, B. Sheehan, J. Lin, P. C. McIntyre, B. Brennan, R. M. Wallace, M. E. Pemble, K. Cherkaoui, *IEEE Trans. Device Mater. Reliab.* **2013**, 13, 429.
- [18] R. Suzuki, N. Taoka, M. Yokoyama, S. Lee, S. H. Kim, T. Hoshii, T. Yasuda, W. Jevasuwan, T. Maeda, O. Ichikawa, N. Fukuhara, M. Hata, M. Takenaka, S. Takagi, *Appl. Phys. Lett.* **2012**, 100, 132906.
- [19] T. Nabatame, K. Iwamoto, H. Ota, K. Tominaga, H. Hisamatsu, T. Yasuda, K. Yamamoto, W. Mizubayashi, Y. Morita, N. Yasuda,

- M. Ohno, in *2003 Symp. VLSI Technology. Digest of Technical Papers (IEEE Cat. No.03CH37407)*, IEEE, Piscataway, NJ, June 2003, pp. 25-26, <https://doi.org/10.1109/VLSIT.2003.1221068>.
- [20] S. Takagi, A. Toriumi, M. Iwase, H. Tango, *IEEE Trans. Electron Devices* **1994**, *41*, 2357.
- [21] D.-H. Ahn, S.-H. Yoon, M. Takenaka, S. Takagi, *Appl. Phys. Express* **2017**, *10*, 084201.
- [22] T. Ando, *Materials* **2012**, *5*, 478.
- [23] Y. Takanashi, K. Takahata, Y. Muramoto, *IEEE Trans. Electron Devices* **1999**, *46*, 2271.
- [24] H.-S. Kang, C.-S. Choi, W.-Y. Choi, D.-H. Kim, K.-S. Seo, *Appl. Phys. Lett.* **2004**, *84*, 3780.
- [25] T. Maeda, K. Oishi, H. Ishii, W. H. Chang, T. Shimizu, A. Endoh, H. Fujishiro, T. Koida, *Appl. Phys. Lett.* **2021**, *119*, 192101, <https://doi.org/10.1063/5.0065776>.
- [26] K. Oishi, H. Ishii, W. H. Chang, H. Ishii, A. Endoh, H. Fujishiro, T. Maeda, *Phys. Status Solidi A* **2021**, *218*, 2000439.
- [27] H. Fang, W. Hu, P. Wang, N. Guo, W. Luo, D. Zheng, F. Gong, M. Luo, H. Tian, X. Zhang, C. Luo, X. Wu, P. Chen, L. Liao, A. Pan, X. Chen, W. Lu, *Nano Lett.* **2016**, *16*, 6416.
- [28] "See <http://www.thorlabs.com> for information about the responsivity of InGaAs and extended InGaAs photodiode (Part No. FD10D)" [https://www.thorlabs.co.jp/\\_sd.cfm?fileName=TTN035386-E0W.html&partNumber=FD10D](https://www.thorlabs.co.jp/_sd.cfm?fileName=TTN035386-E0W.html&partNumber=FD10D) (accessed: December 2023).